Science Advances
AAAS

advances.sciencemag.org/cgi/content/full/6/15/eaay0076/DC1

Supplementary Materials for

The surface stress of biomedical silicones is a stimulant of cellular response

Zhu Cheng, Carolyn R. Shurer, Samuel Schmidt, Vivek K. Gupta, Grace Chuang, Jin Su, Amanda R. Watkins, Abhishek Shetty, Jason A. Spector, Chung-Yuen Hui, Heidi L. Reesink, Matthew J. Paszek*

*Corresponding author. Email: mjp31@cornell.edu

Published 10 April 2020, *Sci. Adv.* **6**, eaay0076 (2020)
DOI: 10.1126/sciadv.aay0076

The PDF file includes:

Other Supplementary Material for this manuscript includes the following:

(available at advances.sciencemag.org/cgi/content/full/6/15/eaay0076/DC1)

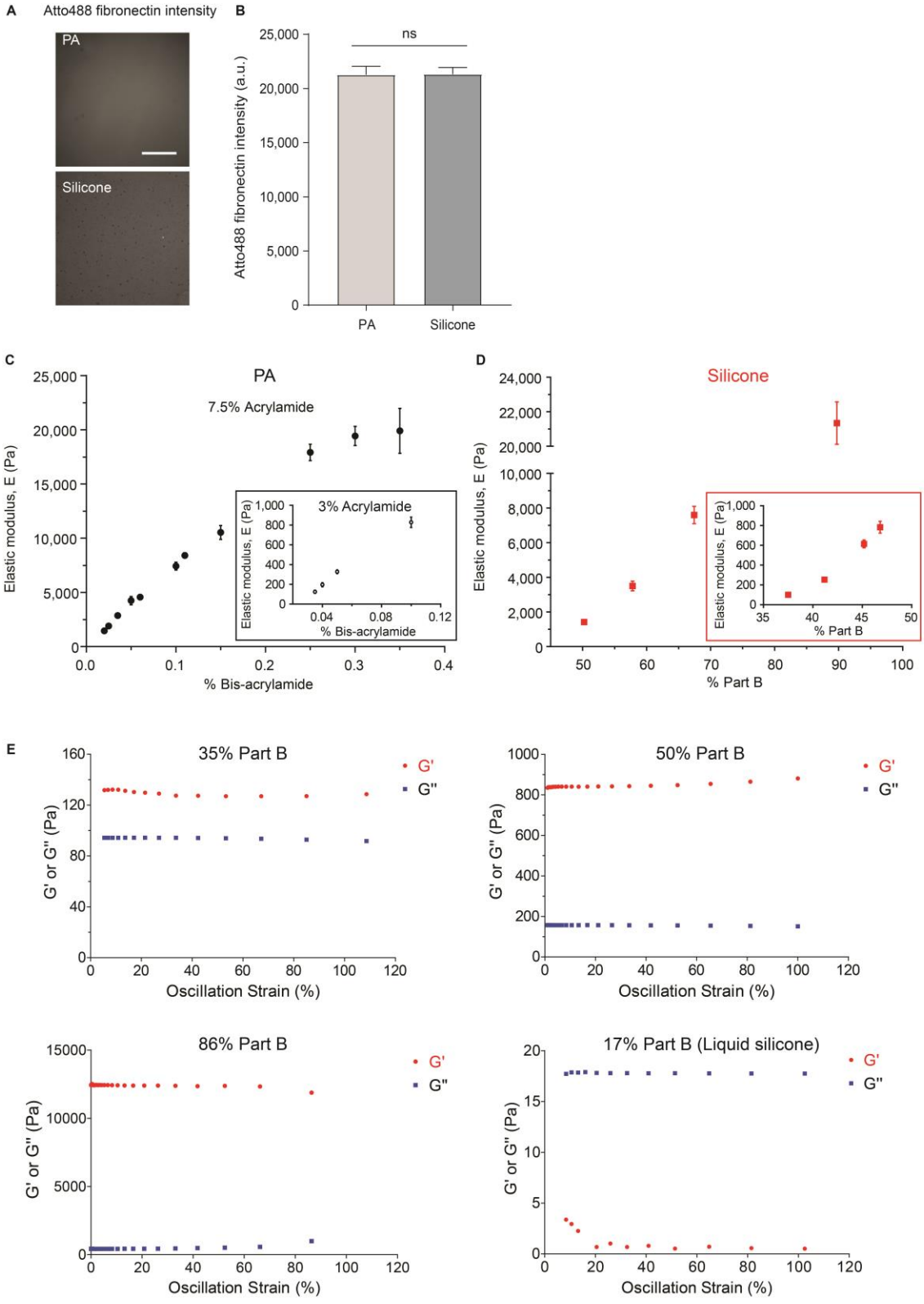

fig. S1. Characterization of PA and silicone substrates. (A) Representative fluorescent images of Atto488-conjugated fibronectin on PA (1 kPa) and silicone (1 kPa) substrates;

scale bar: 100 μm. (B) Average Atto488 intensity recorded on the substrate surface; n $\geqslant$ 9 for each condition; ns, not significant, t test; error bars show standard deviation of the mean. (C) Elastic moduli of polyacrylamide (PA) gels with various acrylamide to bis-acrylamide ratios measured by dynamic mechanical thermal analysis (DMTA). 7-9 independent samples were tested for each point. (D) Elastic moduli of silicone substrates with varying proportions of base silicone to curing reagent measured by DMTA. 7-9 independent samples were tested for each point. Error bars show standard deviation of the mean. (E) Storage and loss moduli of silicone substrates with varying proportions of base silicone to curing reagent. 3 independent samples were tested for each condition.

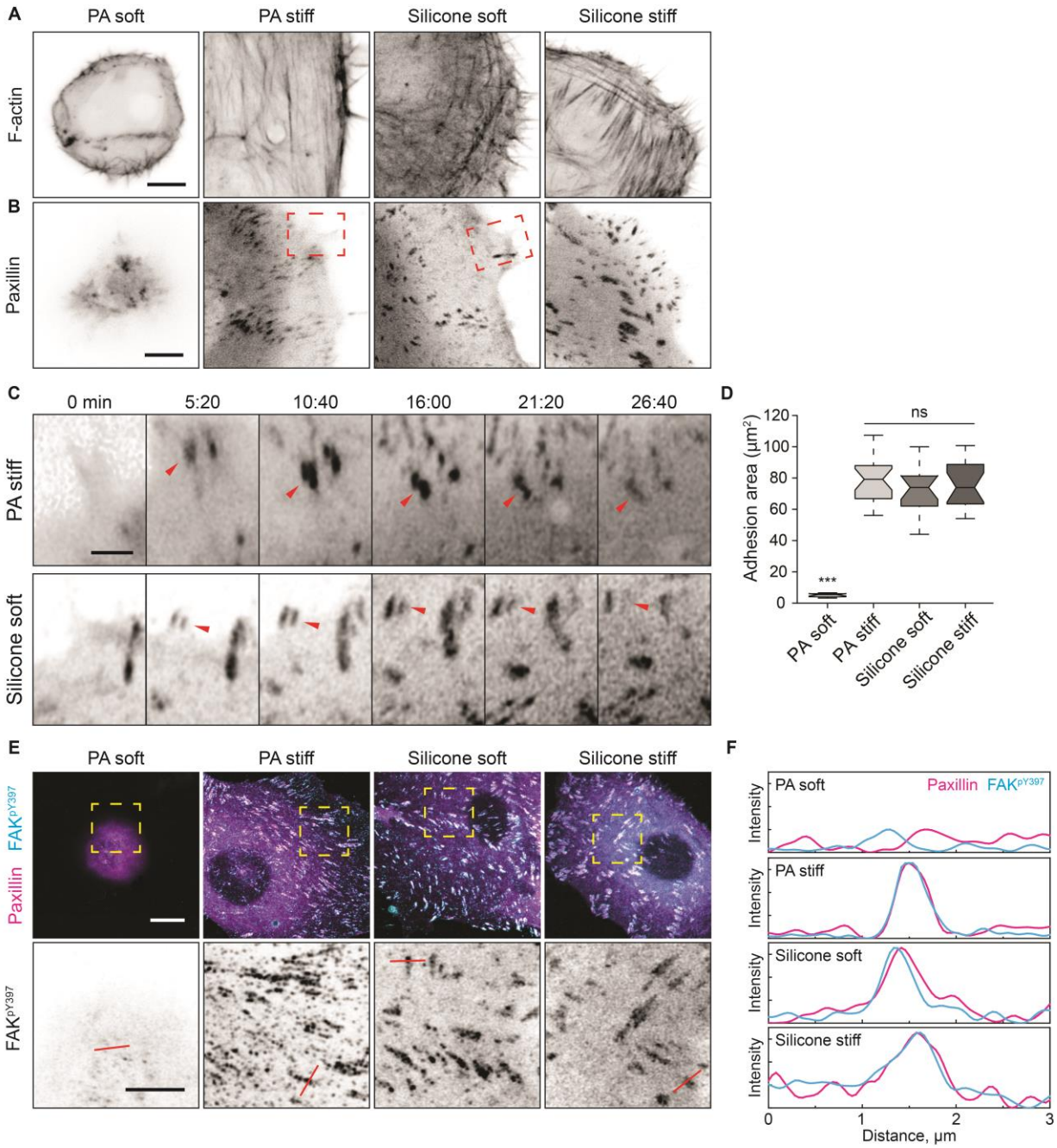

fig. S2. Substrate surface tension activates canonical integrin rigidity sensing pathways. (A) Representative images of filamentous actin in MECs expressing F-tractin-EGFP and grown on the indicated substrates; scale bar, 5 μm. (B) Representative images of adhesions in MECs expressing Paxillin-mCherry and grown on the indicated substrates; scale bar, 5 μm. (C) Representative time-lapse sequences of focal adhesion dynamics in

Paxillin-mCherry expressing MECs on stiff PA (top) and soft silicone (bottom) substrates in the regions indicated in (B); red arrowheads show representative life cycles of adhesion complexes; scale bar, 2 μm. (D) Quantification of adhesion area for MECs on the indicated substrates as described in (B). *** $p<0.001$, ns, not significant, t-test; $n > 20$ for each condition. Horizontal lines are medians, boxes show the interquartile range (IQR), whiskers extend to minimum and maximum values. (E) Representative immunofluorescence images of Paxillin and activated focal adhesion kinase (pY397) in MECs on the indicated gels. Dashed yellow rectangle designates region shown with FAK^{pY397} channel isolated. Scale bars, 10 μm (top), 5 μm (bottom). (F) Intensity of pixels along the red lines shown in (E) (bottom panels). Magenta, Paxillin channel; Cyan, FAK^{pY397} channel. PA soft: 0.12 kPa; PA stiff: 20 kPa; Silicone soft: 0.1 kPa; Silicone stiff: 21 kPa.

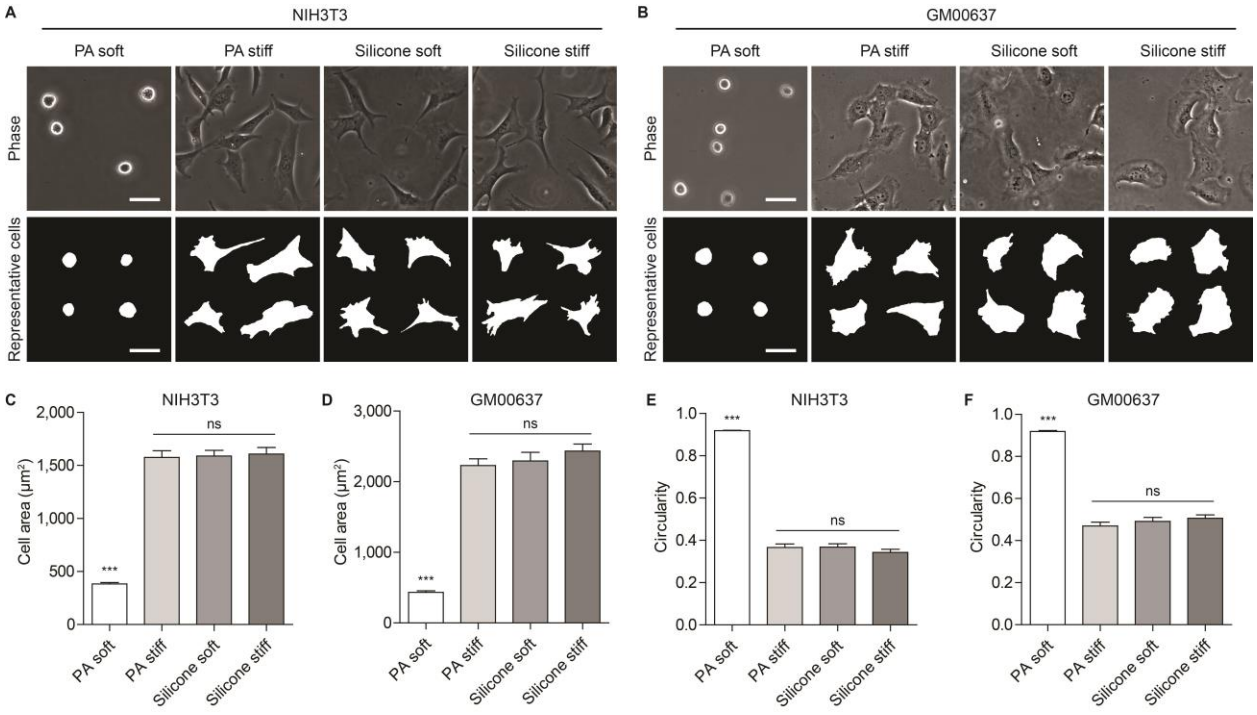

fig. S3. Relationship between fibroblast morphology and substrate elastic modulus.

(A, B) Representative phase contrast images and cell masks of (A) mouse NIH3T3 fibroblasts and (B) human GM00637 fibroblasts on the indicated substrates; scale bars: 50 μm. PA soft: 0.12 kPa; PA stiff: 20 kPa; Silicone soft: 0.1 kPa; Silicone stiff: 21 kPa. (C, D) Quantification of cell spread area of (C) NIH3T3 fibroblasts and (D) GM00637 fibroblasts on the substrates. *** $p<0.001$, ns, not significant, t-test; $n > 42$ cells per condition. (E, F) Quantification of cell circularity of (E) NIH3T3 fibroblasts and (F) GM00637 fibroblasts on the substrates. *** $p<0.001$, ns, not significant, t-test; $n > 42$ cells per condition. Error bars show standard error of the mean.

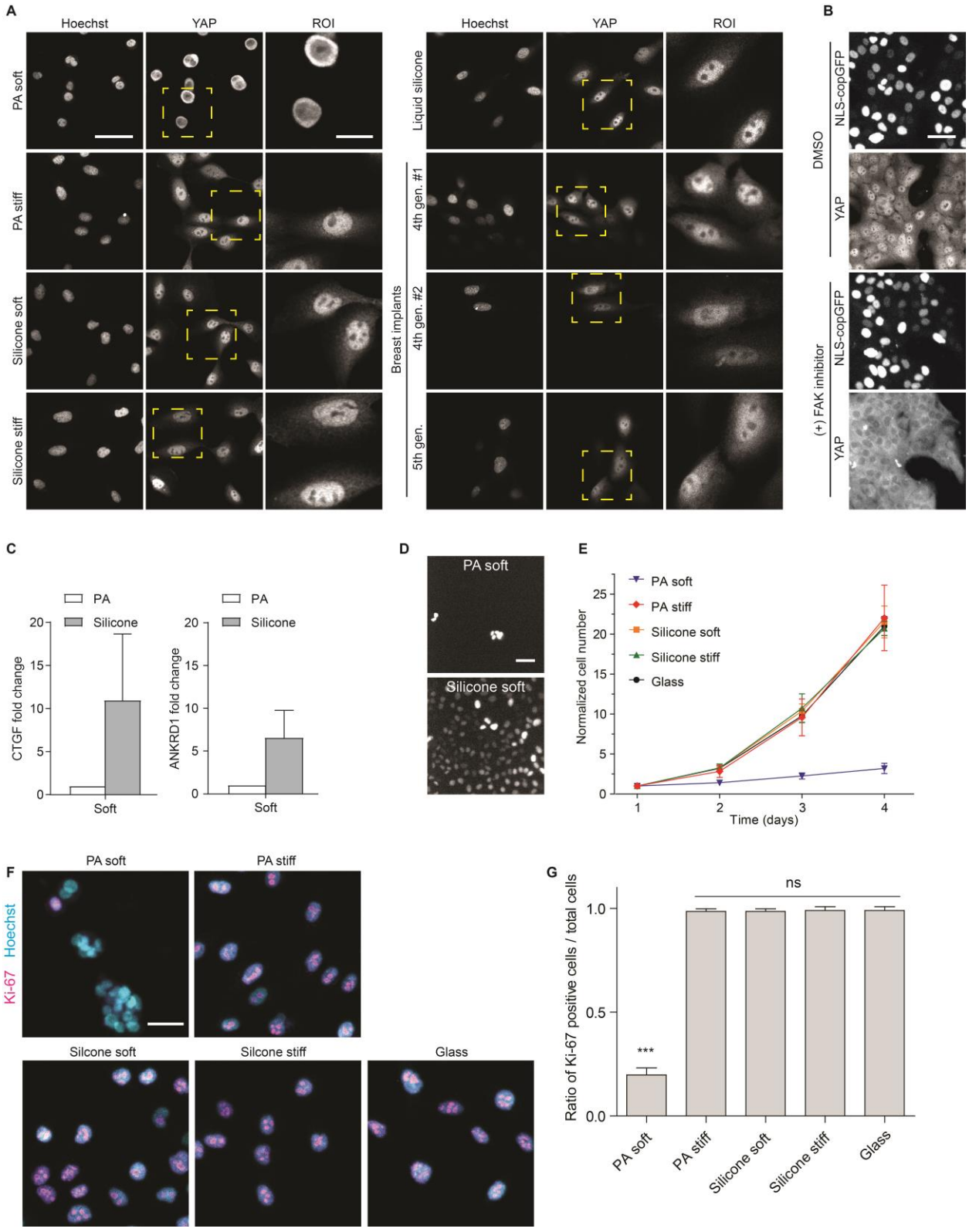

fig. S4. Substrate surface tension promotes cell proliferation and directs YAP/TAZ-mediated gene expression. (A) Representative images of nuclei and YAP localization in

MECs grown on the indicated substrates; experiments conducted in triplicate. Scale bars are 50 μm and 20 μm in the ROI. TCPS: tissue culture polystyrene; Three types of silicone breast implants: 4th generation #1, 4th generation #2, and 5th generation. ns, not significant, t-test; $n > 4$. (B) Representative images of YAP localization on glass substrates; cells are serum starved overnight, treated with DMSO control or 5 μM PF-573228 (FAK inhibitor) for two hours, then stimulated with EGF for 20 minutes; $n = 3$; scale bar: 50 μm. (C) Relative fold change in CTGF and ANKRD1 gene expression on soft PA and silicone gels; $n = 3$. All error bars show standard error of the mean. (D) Fluorescence images of MECs expressing nuclear located GFP on compliant PA and silicone substrates four days after seeding; scale bar, 50 μm. (E) Quantification of MECs growing on glass, soft and stiff silicone gels, soft and stiff PA gels from day 1 to day 4 after seeding; data normalized to day one. (F) Representative immunofluorescence images of Ki-67 in MECs on the indicated gels. (G) Ratio of the number of Ki-67 positive cells over total number of cells. At least 115 cells were analyzed for each condition; *** $p < 0.0001$, ns, not significant, t-test; scale bar: 30 μm.

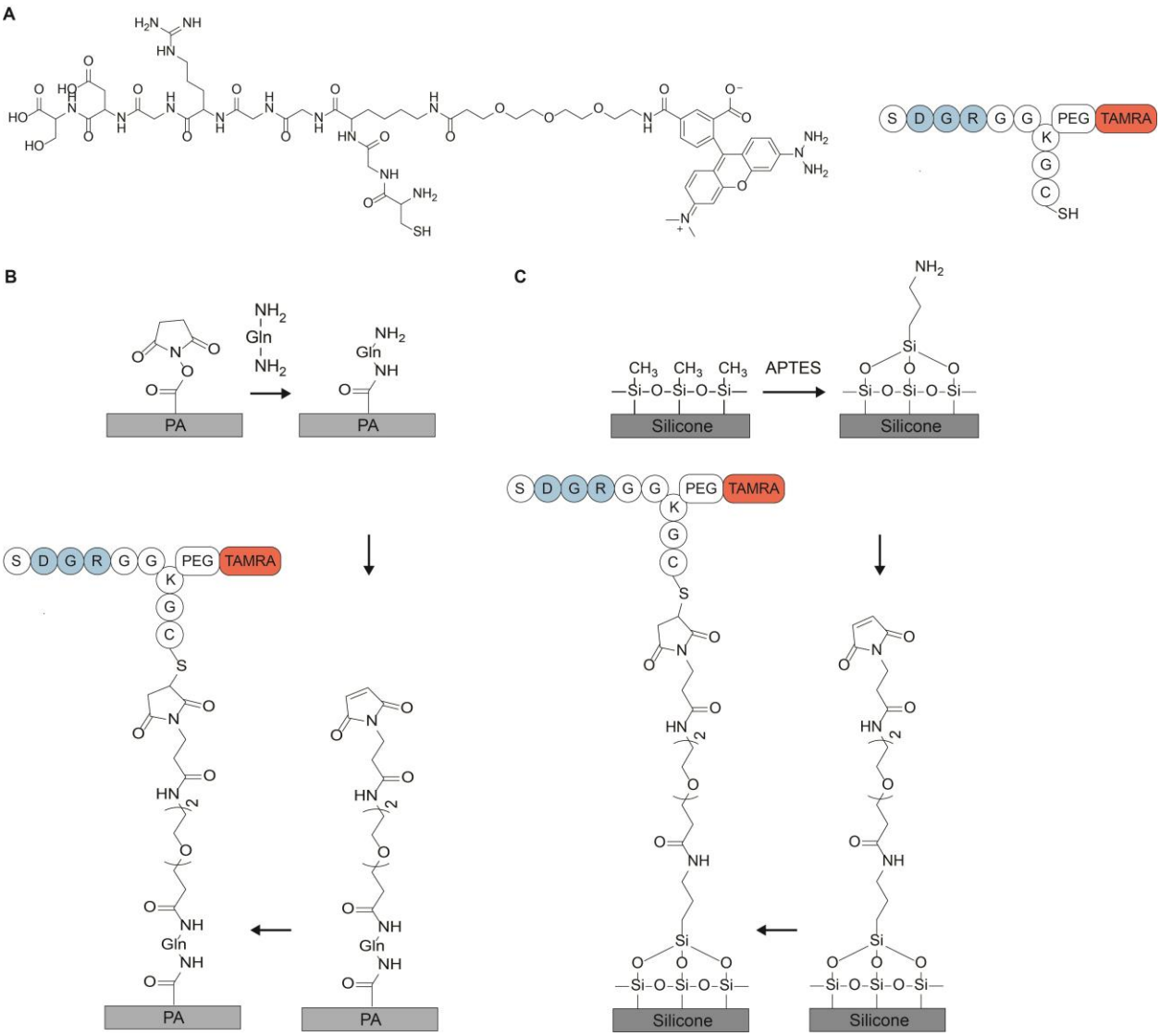

fig. S5. Surface conjugation of TAMRA-tagged RGD peptide onto the substrates. (A) Left: molecular structure of the TAMRA-RGD peptide. Right: simplified schematic showing the structure of TAMRA-RGD peptide. (B) Diagram for the covalent attachment of TAMRA-RGD to the surface of PA substrates. (C) Diagram for the covalent attachment of TAMRA-RGD to the surface of silicone substrates. NH_2-Gln-NH_2, glutamine; APTES, (3-Aminopropyl)-triethoxysilane.

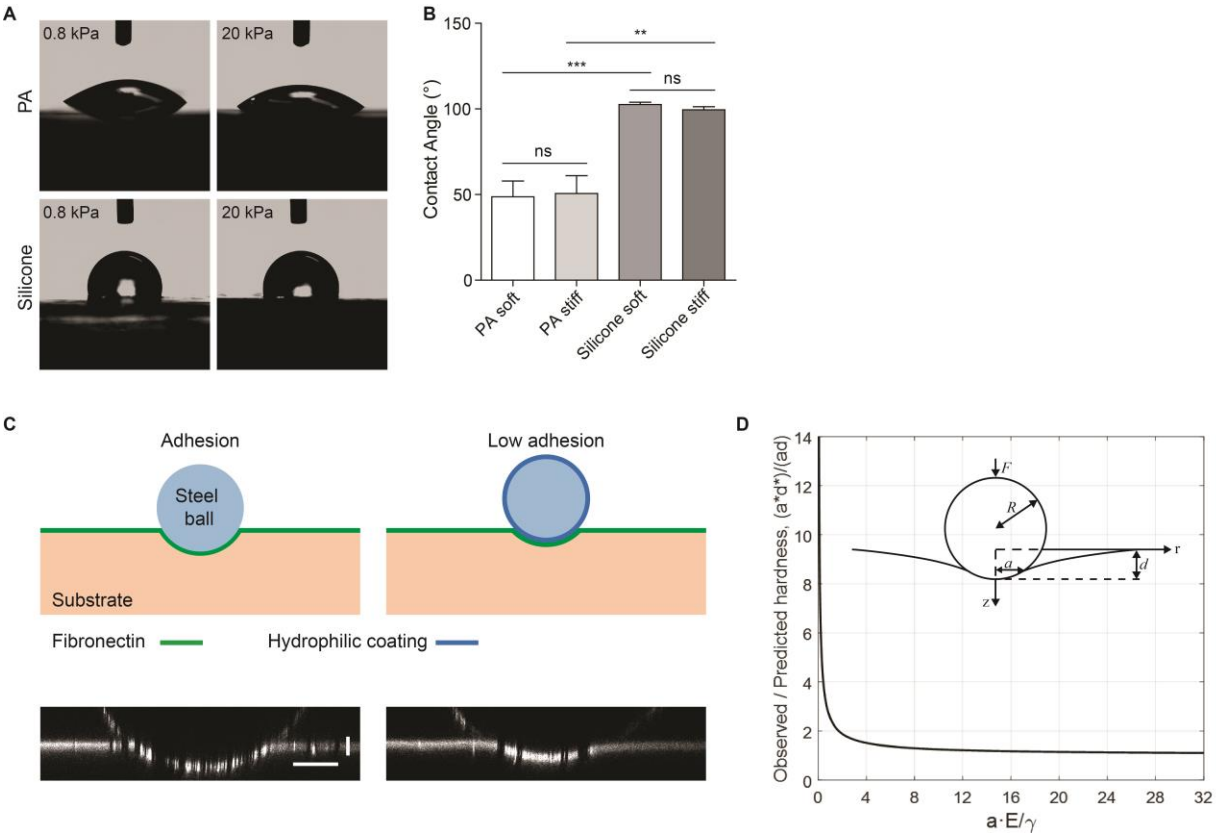

fig. S6. Substrate surface energy and model of contact mechanics with surface tension. (A) Contact angle measurements on fibronectin-conjugated PA and silicone substrates of the indicated elastic modulus. (B) Quantified contact angles of water droplets on PA and silicone materials. *** $p<0.001$, ** $p<0.005$, ns, not significant, t-test, more than 5 independent samples were analyzed for each condition. PA soft: 0.8 kPa; PA stiff: 20 kPa; Silicone soft: 0.8 kPa; Silicone stiff: 20 kPa. *** $p<0.001$, t-test; n = 4. Error bars show standard error of the mean. (C) Top: Schematics depicting the indentation of steel balls into substrates. Steel balls were untreated or treated with a hydrophilic polymer coating, and substrates were conjugated with fibronectin. Left and right panels indicate adhesive contact between naked steel balls and substrates and negligible adhesion between coated steel balls and substrates. Bottom: confocal fluorescent images showing the corresponding surface profiles of adhesive and low adhesive contacts. Steel ball radius, 254 μm; horizontal

scale bar, 100 μm; vertical scale bar, 30 μm. (D) Ratio of observed hardness over Hertz predicted hardness, a*d*/(ad), versus the elasto-capillary number, a·E/γ from the mathematical model of modified contact mechanics with surface tension; a* and d* are the Hertz predicted contact radius and indentation depth, respectively. Insert: Schematic depicting the indentation of a rigid indenter into an elastic substrate.

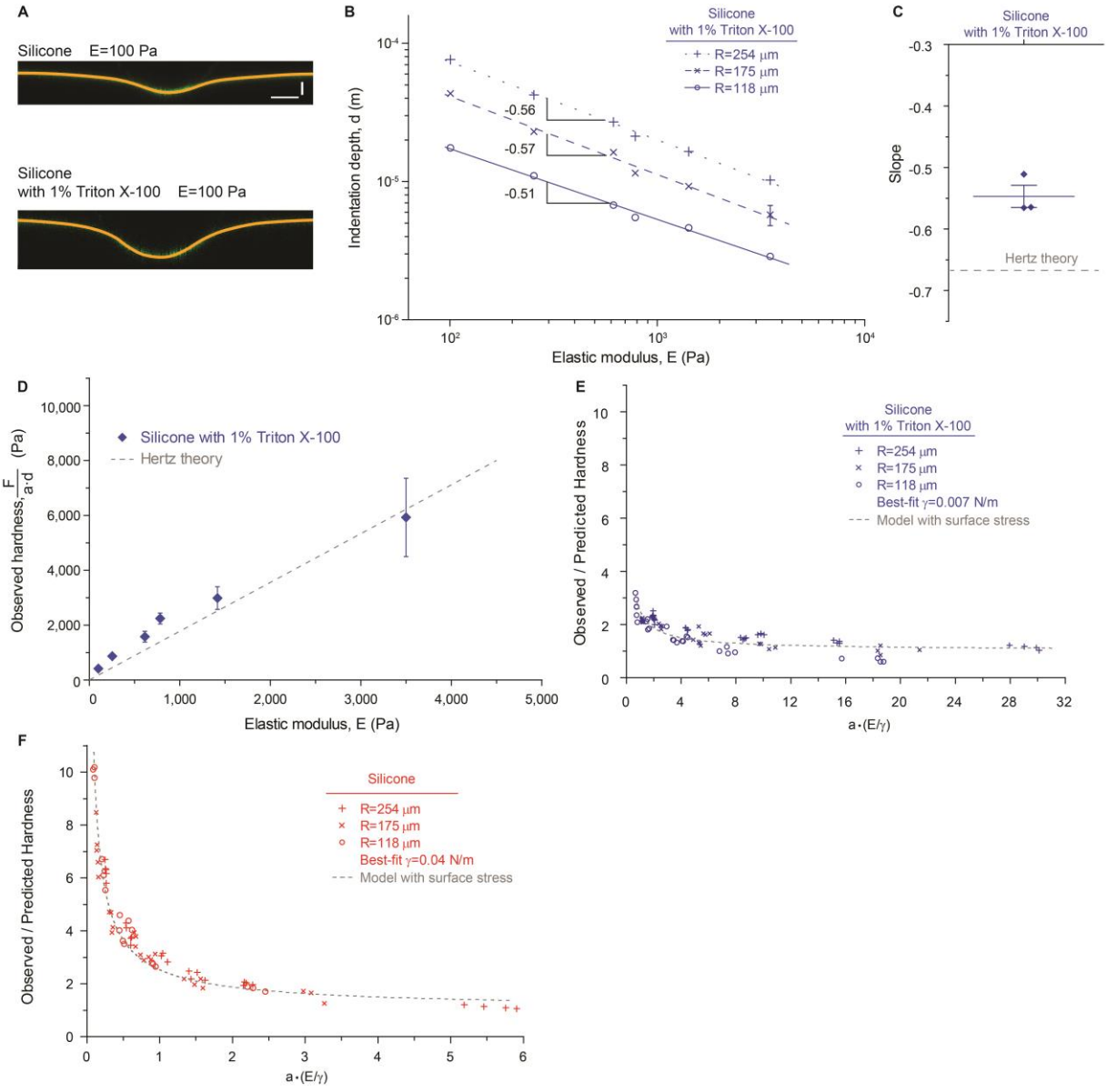

fig. S7. Surfactant reduces the surface tension of biomaterials. (A) Confocal fluorescent images showing the surface profiles of silicone gels submerged in buffer (top) and buffer with surfactant (bottom), and indented by steel balls with radii of 254 μm; horizontal scale bar, 100 μm; vertical scale bar, 30 μm. (B) Indentation depth of the steel ball, d, versus substrate elastic modulus, E, for silicone substrates submerged in buffer with surfactant; steel ball radii as indicated, 254 μm, 175 μm, or 118 μm; error bars show standard error of the mean. (C) Slopes of the log-log scale plots shown in panel (B); error bars represent

standard error of the mean. (D) Observed substrate hardness, $F/(a \cdot d)$, versus elastic modulus, E; F is the indentation force and a is the measured contact radius of the indenter; dashed line shows the prediction by Hertz contact theory; $n \geqslant 12$. (E) Zoom-in of Fig. 3F. Ratios of observed hardness over predicted hardness versus the non-dimensional parameter, $a \cdot (E/\gamma)$, for silicone gels submerged in buffer with surfactant; best-fit surface tension, γ, is 0.007 N/m for gel in buffer with surfactant. (F) Zoom-in of Fig. 3F. Ratios of observed hardness over predicted hardness versus the non-dimensional parameter, $a \cdot (E/\gamma)$, for silicone gels submerged in buffer; best-fit surface tension, γ, is 0.04 N/m for gel in buffer.

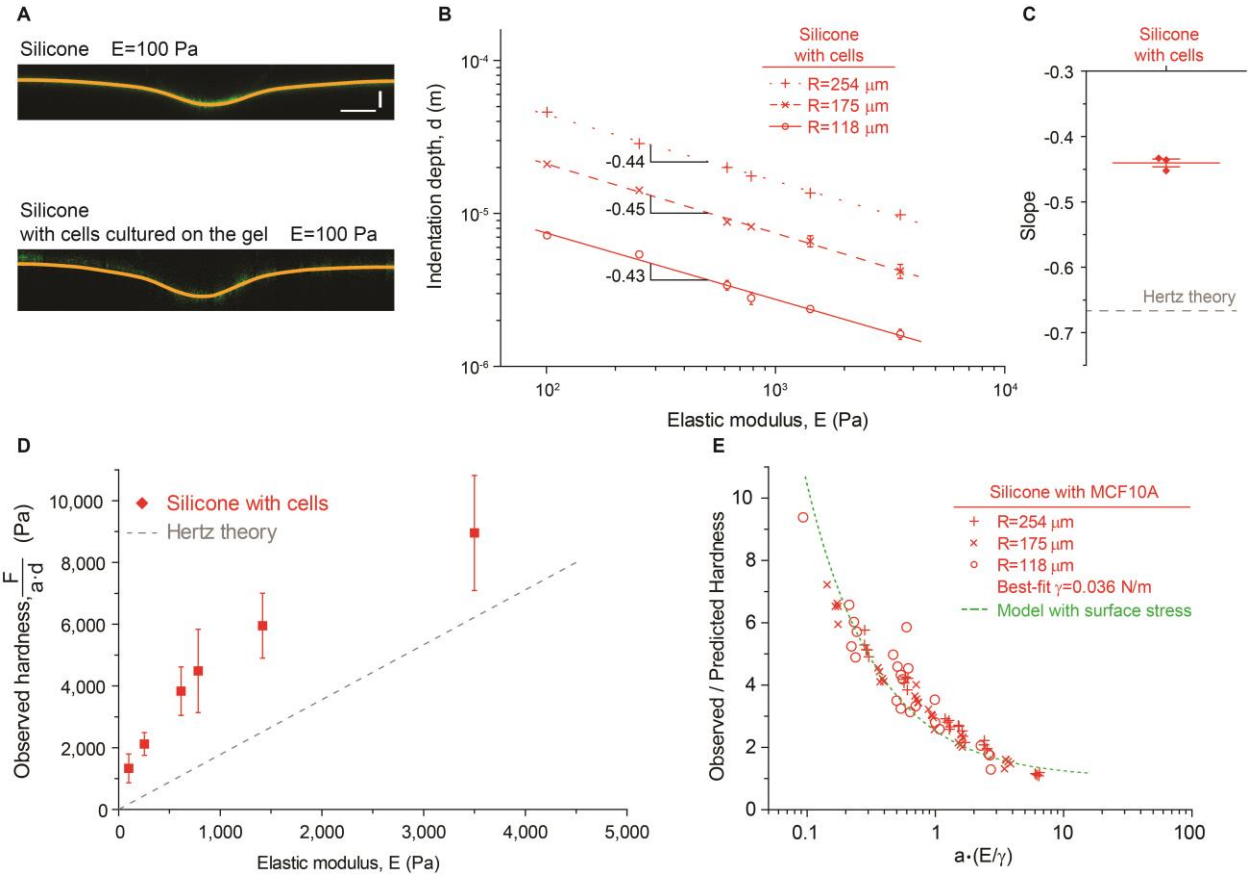

fig. S8. Characterization of surface tension of biomaterials following cell culture. (A) Confocal fluorescent images showing the surface profiles of silicone gels submerged in buffer (top) and cell culture media with cells cultured on the gel (bottom), and indented by steel balls with radii of 254 μm; horizontal scale bar, 100 μm; vertical scale bar, 30 μm. (B) Indentation depth of the steel ball, d, versus substrate elastic modulus, E, for silicone substrates submerged in cell culture media with cells cultured on the gel; steel ball radii as indicated, 254 μm, 175 μm, or 118 μm; error bars show standard error of the mean. (C) Slopes of the log-log scale plots shown in panel (B); error bars represent standard error of the mean. (D) Observed substrate hardness, F/(a·d), versus elastic modulus, E; F is the indentation force and a is the measured contact radius of the indenter; dashed line shows the prediction by Hertz contact theory; n ⩾ 12. (E) Ratios of observed hardness over

predicted hardness versus the non-dimensional parameter, $a \cdot (E/\gamma)$, for silicone gels submerged in cell culture media with cells cultured on the gel; best-fit surface tension, γ, is 0.036 N/m.

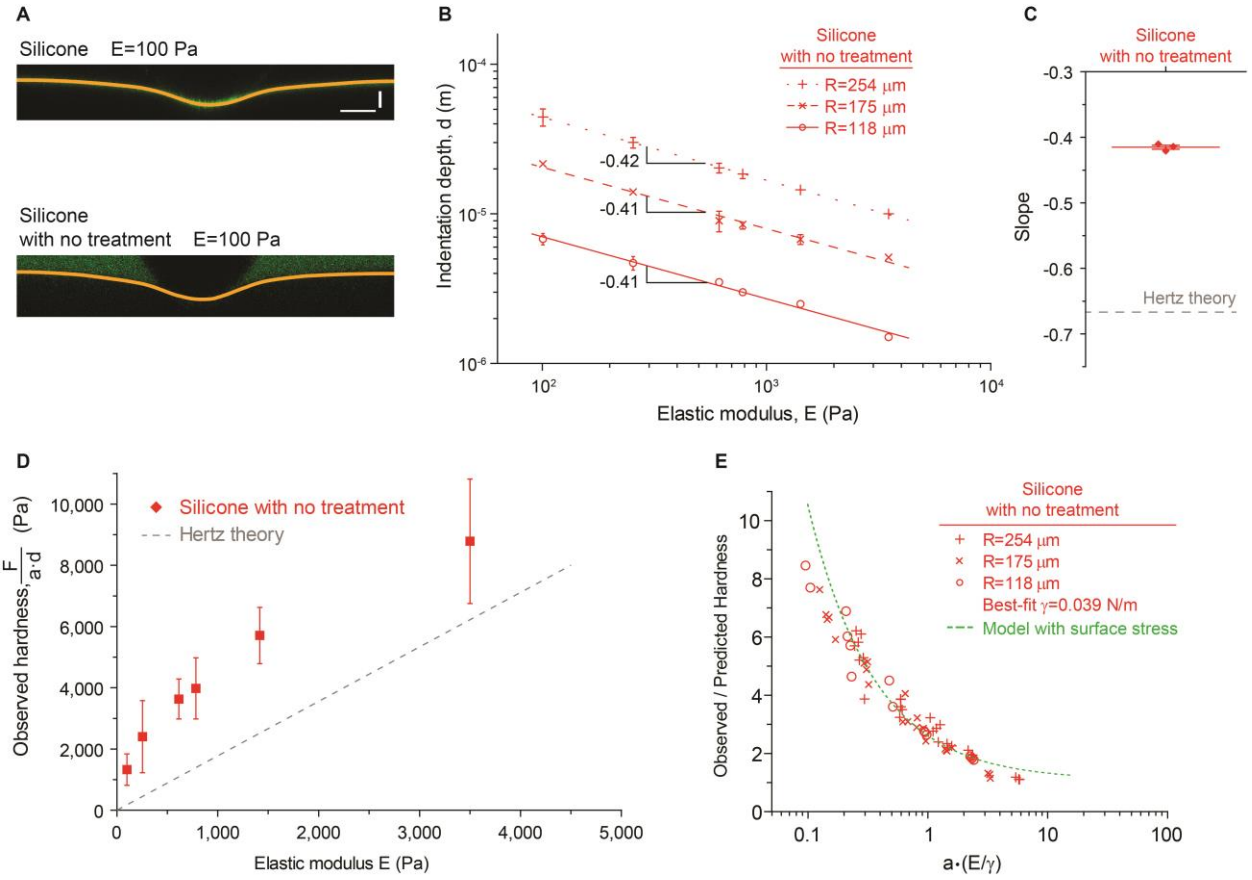

fig. S9. Characterization of surface tension of biomaterials without adsorbed fibronectin. (A) Confocal fluorescent images showing the surface profiles of silicone gels adsorbed with Atto488 fibronectin (top) and without adsorbed fibronectin (bottom; imaged in PBS buffer with free Atto488 for contrast), and indented by steel balls with radii of 254 μm; horizontal scale bar, 100 μm; vertical scale bar, 30 μm. (B) Indentation depth of the steel ball, d, versus substrate elastic modulus, E, for silicone substrates submerged in buffer with no surface fibronectin treatment; steel ball radii as indicated, 254 μm, 175 μm, or 118 μm; error bars show standard error of the mean. (C) Slopes of the log-log scale plots shown in panel (B); error bars represent standard error of the mean. (D) Observed substrate hardness, F/(a·d), versus elastic modulus, E; F is the indentation force and a is the measured contact radius of the indenter; dashed line shows the prediction by Hertz contact

theory; $n \geqslant 12$. (E) Ratios of observed hardness over predicted hardness versus the non-dimensional parameter, $a \cdot (E/\gamma)$, for silicone gels submerged in buffer with no surface fibronectin treatment; best-fit surface tension, γ, is 0.039 N/m.

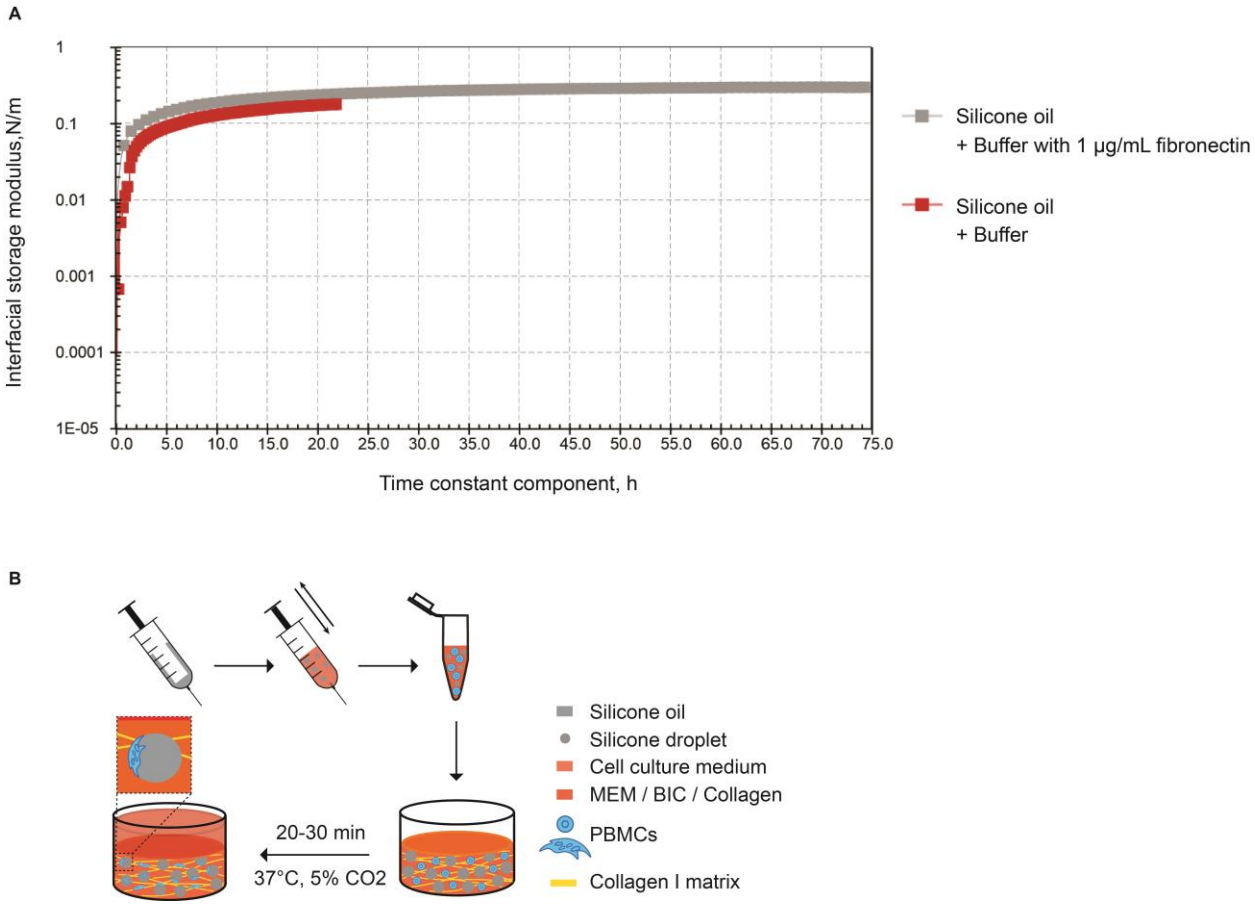

fig. S10. Interfacial rheology of silicone oil and the workflow of investigating the interaction of PBMCs and silicone oil droplets. (A) Interfacial storage modulus of the interface between silicone oil and buffer (PBS) or buffer supplemented with 1 µg/mL fibronectin; experiments performed at 25°C. The interfacial loss modulus was negligible for each condition and not illustrated. (B) A schematic workflow depicting a biomimetic culture assay for investigating the interactions between PBMCs and silicone oil droplets. Silicone micro-droplets suspended in media were prepared by mixing silicone oil with media in a syringe plunger. Suspended droplets were then mixed with previously prepared collagen I mastermix and cells in a tube on ice, followed by polymerization of the collagen gel in a 96-well plate.

Supplemental Movies

Movie S1. Adhesion between silicone substrates and uncoated steel balls. Naked steel ball adhering to a fibronectin-conjugated silicone substrate.

Movie S2. Minimal adhesion between silicone substrates and steel balls prepared with hydrophilic polymer coatings. Coated steel ball rolling on a fibronectin-conjugated silicone substrate.

Movie S3. Focal adhesion dynamics in cells migrating on stiff PA substrates. Confocal microscopy time-lapse images of MECs expressing Paxillin-mCherry and migrating on stiff PA gels. Images were acquired every 80 sec for 19 min; scale bar, 10 μm.

Movie S4. Focal adhesion dynamics in cells migrating on soft silicone substrates. Confocal microscopy time-lapse images of MECs expressing Paxillin-mCherry and migrating on soft silicone gels. Images were acquired every 80 sec for 36 min; scale bar, 10 μm.

Movie S5. Focal adhesion dynamics in cells migrating on stiff PA substrates. Confocal microscopy time-lapse images of MECs expressing Paxillin-mCherry and migrating on stiff PA gels. Images were acquired every 80 sec for 21 min; scale bar, 2 μm.

Movie S6. Focal adhesion dynamics in cells migrating on soft silicone substrates.

Confocal microscopy time-lapse images of MECs expressing Paxillin-mCherry and migrating on soft silicone gels. Images were acquired every 80 sec for 27 min; scale bar, 2 μm.